Optics Letters

Speckle-based x-ray phase-contrast imaging with a laboratory source and the scanning technique

Tunhe Zhou,[1,*] Irene Zanette,[2,3] Marie-Christine Zdora,[2] Ulf Lundström,[1,4] Daniel H. Larsson,[1] Hans M. Hertz,[1] Franz Pfeiffer,[2,5] and Anna Burvall[1]

[1]Biomedical and X-ray Physics, KTH Royal Institute of Technology, Albanova, SE-10691, Stockholm, Sweden
[2]Physik-Department & Institut für Medizintechnik, Technische Universität München, 85748 Garching, Germany
[3]Diamond Light Source, Harwell Science and Innovation Campus, Didcot, OX11 0DE, UK
[4]Stanford University, Department of Structural Biology, Stanford, California 94305, USA
[5]Institut für Diagnostische & Interventionelle Radiologie, Technische Universität München, 81675 München, Germany
*Corresponding author: tunhe.zhou@biox.kth.se

Received 27 March 2015; revised 23 May 2015; accepted 27 May 2015; posted 27 May 2015 (Doc. ID 237037); published 10 June 2015

The speckle-based scanning method for x-ray phase-contrast imaging is implemented with a liquid-metal-jet source. Using the two-dimensional scanning technique, the phase shift introduced by the object is retrieved in both transverse orientations, and the limitations on spatial resolution inherent to the speckle-tracking technique are avoided. This method opens up possibilities of new high-resolution multimodal applications for lab-based phase-contrast x-ray imaging.

OCIS codes: (340.7440) X-ray imaging; (110.7440) X-ray imaging; (030.6140) Speckle; (110.6150) Speckle imaging.

http://dx.doi.org/10.1364/OL.40.002822

X-ray phase-contrast imaging has seen rapid development over the last decade due to its advantages in imaging of low-absorbing objects, such as soft tissue, compared to conventional attenuation x-ray imaging. Among different phase-contrast imaging methods, propagation-based imaging (PBI) [1], grating-based imaging (GBI) [2], and speckle-based imaging (SBI) [3] adapt well to polychromatic light and hence to laboratory sources. SBI exists in different versions: single-shot speckle tracking [3–5] and speckle scanning [6]. Moreover, since it relies on the analysis of the sample-induced changes of a structured intensity pattern in the near-field or holographic regimes, near-field ptychography can also be considered part of the SBI methods [7,8].

SBI techniques use an experimental arrangement with some similarity to that of PBI, but they use a random phase modulator (static diffuser) to generate a near-field speckle pattern. SBI does not require any sophisticated and strongly absorbing optical elements and can be implemented with, e.g., a membrane or sandpaper. When an object is placed in the beam, the speckle pattern will be disturbed. The single-shot speckle-tracking technique, recently implemented with a laboratory source [9], compares the speckle patterns with and without object-using correlation analysis. It generates information on the phase gradient of the sample, but also on the absorption and scattering information in two dimensions. Unlike PBI, SBI can quantitatively retrieve the complex refractive indices of multiple-material samples when combined with tomography, without need for prior knowledge of the sample materials.

The speckle-scanning technique used in the present Letter [6] is based on a principle similar to two-dimensional GBI [10], but replaces the phase-stepped grating with a diffuser. As the correlation analysis is done on 2D scan data for each pixel, the speckle-scanning method gives higher spatial resolution than the speckle-tracking method, where subsets containing many pixels are used for correlation. The cost for the high resolution of the speckle-scanning method is a large number of images, which means a longer exposure time.

Our experimental arrangement is schematically represented in Fig. 1. The source [11] has a galinstan jet anode and generates a spot size with a full width at half maximum (FWHM) of 6 μm × 8 μm, which gives sufficient spatial coherence for SBI. The static diffuser used is a piece of P800 sandpaper with a grit size of about 22 μm, which is mounted on a two-dimensional linear stage for 2D raster scan. The CCD

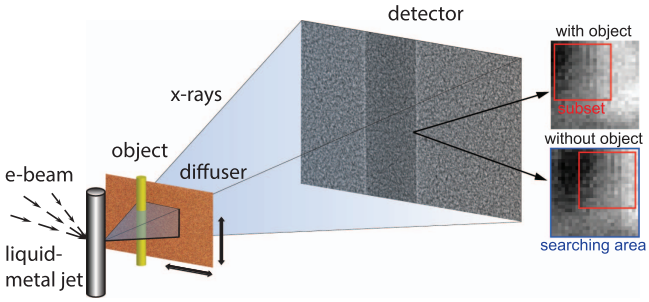

Fig. 1. Experimental arrangement and correlation principle for the speckle-scanning technique. From the pixel map with object a subset is chosen, and then located in the searching area in the pixel map without object.

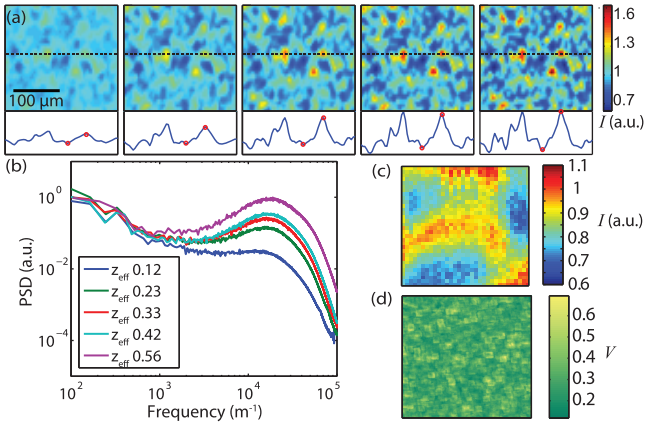

Fig. 2. (a) Normalized speckle pattern at five different detecting positions, and the profiles taken at the dashed lines. (b) Power spectral density (PSD) of the speckle images. (c) Normalized intensity pattern of a 32 × 32 steps scan of one random pixel. (d) Visibility map in a 200 × 200 pixels region of the speckle scan.

scintillator detector has a pixel size of 9 μm, and the FWHM of the point-spread function (PSF) is about 22 μm. For each pixel, two sets of data are collected through the scan: with and without objects, as illustrated in the insets in Fig. 1. If we assume that the local phase varies slowly, this implies a rigid transverse position shift without distortion of the pattern. Then we can match the scan pattern with and without object including some displacement. Correlation analysis can be used to find the size of the position shift, and therefore the phase gradient of the object.

Speckle characteristics such as visibility and size are important to the resulting image quality. To characterize the speckle properties using the liquid-metal-jet source, five speckle images were collected at five different propagation distances and presented in Fig. 2(a). The diffuser is 0.76 m from the source, and for the images from left to right, the detector stands 0.90 m, 1.10 m, 1.35 m, 1.75 m, and 2.86 m from the source, respectively. The acquisition time is adjusted (longer for longer distance) to keep the total photon count and therefore the noise level similar. Since the x-rays are filtered by different lengths of air, the mean energy for the five distances is in the range of 16–21 keV. For plane-wave illumination, speckle size would not change with distance [12]. As we have a spherical wavefront, speckle size changes by the geometrical magnification $M = (R_1 + R_2)/R_1$, where R_1, R_2 is the source-to-diffuser and diffuser-to-detector distance, respectively. In the images, the geometrical magnification is compensated for, and the intensities normalized (or flatfield-corrected). The effective-propagation distances $z_{\mathrm{eff}} = R_2/M$ for the five images are 0.12 m, 0.23 m, 0.33 m, 0.42 m, and 0.56 m, respectively. It can be seen that the speckle shape and size do not change, but the visibility increases with z_{eff}, which complies with the observations from [12]. The speckle visibility, evaluated as $V = (I_{\max} - I_{\min})/2\overline{I}$, where $\overline{I}$ is the mean intensity, and $I_{\max}$ and $I_{\min}$, are taken along the line indicated in Fig. 2(a) and shown as red circles, is 9%, 16%, 24%, 29%, and 34%, respectively. Shown in Fig. 2(b), the azimuthally-averaged power spectral densities (PSD) of the five speckle images are calculated as [13]

$$\mathrm{PSD}(k) = \left| \int_{-\infty}^{\infty} f(r) e^{-2\pi i r k} \mathrm{d}r \right|^2, \quad (1)$$

where k is the spatial frequency, and $f(r)$ represents the speckle intensity function along the radial axis as we assume that the speckles are circularly symmetric. The different magnifications are compensated for. The peaks of the PSD lines are all at around 1.8×10^4 m^{-1}, corresponding to a pattern structure of 56 μm, which matches direct observation of the speckles. The speckle pattern is determined by the static diffuser's structure, as well as the contrast transfer function of the wavefront, the detector PSF, and the source coherence function. In Fig. 2(c), the intensity pattern of one random pixel from a scan is presented with a visibility of 43%. The distance from source to diffuser is 0.76 m and from source to detector 1.75 m. The diffuser is scanned in two dimensions for 32 × 32 steps with a step size of 1 μm. The visibility map of a 200 × 200 pixels region for this scan is presented in Fig. 2(d), where V varies from 12% to 69%. Because the scan range does not cover more than one speckle and the speckles are randomly distributed, the scan pattern intensity can be very different for different pixels, and therefore the visibility varies.

In this Letter, two samples were imaged. Figure 3 shows an experimental result for an object made of poly(methyl methacrylate) (PMMA) and polystyrene (PS) spheres in a polyvinyl chloride (PVC) tube. The diameters of the PS sphere are 250–350 μm and of the PMMA spheres around 80 μm. The object is placed 0.4 m, the sandpaper 0.8 m, and the detector 1.6 m from the source, which makes z_{eff} 0.4 m for the diffuser. The source is operated with 50-kV acceleration voltage

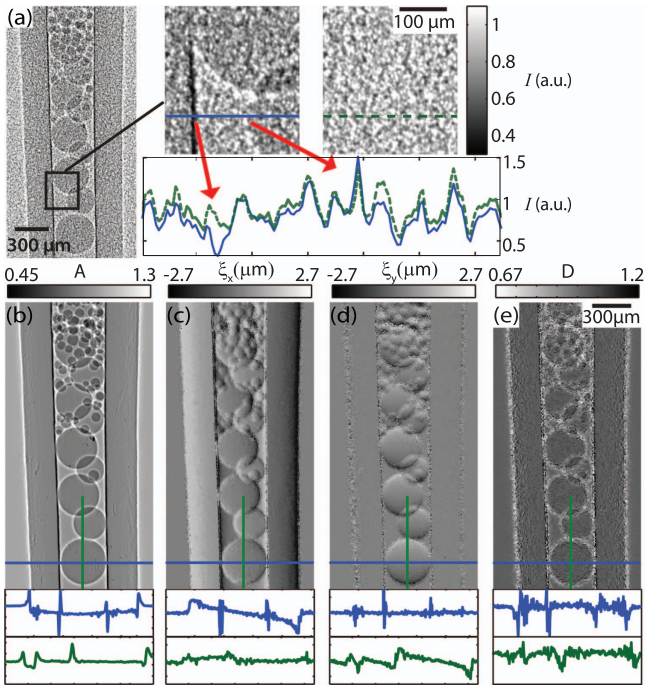

Fig. 3. (a) One experimental image of a phantom made of PS (250–350 μm) and PMMA (~80 μm) spheres in a PVC tube, and its enlarged ROI showing the varied speckle pattern caused by the object. (b) The attenuation A, (c),(d) the transverse shift ξ_x and ξ_y, and (e) the dark-field image D of the object; the profiles are taken at the lines marked in each image.

and 0.8-mA tube current. The scan has 30 × 30 steps with a step size of 0.9 μm in x and y directions and an exposure time of 1 min per step, which gives a total exposure time (with and without object) of 30 h. One row of reference scans without object was taken after every row of sample scans to reduce the variation between reference and sample images caused by equipment or source drift. Figure 3(a) shows a sample image recorded during the scan, in which a region of interest (ROI) of 127 × 141 pixels, which corresponds to 286 μm × 317 μm in the object plane, is marked. The enlarged ROI and the same region in the reference image are presented, as well as one profile plot from each of them. We can observe the attenuation and shift of the speckles introduced by the object, as well as a bit of distortion at the object edges, as indicated by the arrows. Figure 3(b) shows the absorption image, which is calculated as the ratio of the detected photons with and without object. The profiles are plotted in the same range as the color bar. For the speckle-scanning method, the average ratio from all steps is used. The result is similar to a PBI projection image with obvious edge enhancement in addition to the absorption information. Figures 3(c) and 3(d) show the transverse shift in x and y direction, respectively, which gives information on the phase gradient of the object. The phase gradient g of the object is approximately proportional to the angular deviation α of the wavefront if assuming α is small, and therefore proportional to the transverse shift ξ of the diffuser as $g = 2\pi\alpha/\lambda = 2\pi\xi/\lambda z_{\text{eff}}$, where λ is the x-ray wavelength. The transverse shift ξ can be deduced either with Fourier analysis as for GBI or through correlation analysis in real space [6]. The Fourier method can be faster, but we chose normalized cross-correlation as it is less sensitive to average intensity change and noise [14]. At the cross-correlation maximum, a 2nd-order polynomial fitting of the neighboring 3 × 3 pixels gives the shift on a subpixel level [15]. From the profiles in Fig. 3(c), we can see that at the object edges some transverse shifts are not found correctly. The inaccurate cross-correlation is caused by pattern distortion that occurs when the local phase varies rapidly, e.g., at the edges. The variation of the scan pattern can be represented by the ratio of the normalized standard deviation (or the coefficient of variation) with and without object. Here we call it the dark-field signal as in [6]

$$D = \frac{\sigma_{\text{samp}}}{\bar{I}_{\text{samp}}} \Big/ \frac{\sigma_{\text{ref}}}{\bar{I}_{\text{ref}}}, \tag{2}$$

where the standard deviation σ and the average value $\bar{I}$ are evaluated on the intensity pattern of the same pixel for the scan with and without sample. Figure 3(e) presents the dark-field image of the phantom sample. The signal is more significant at the edges as the samples are homogenous without inner structure.

The technique was also applied on a dried spider sample shown in Fig. 4. The diffuser is 76 cm, the object 87 cm, and the detector 175 cm from the source, which gives the object a magnification of 2. The source operates at a voltage of 50 kV and with a current of 0.6 mA. The exposure time is 1 min per frame under a 32 × 32 raster scan with a 1-μm step size, giving a total exposure time of 34 h. Figure 4(b) shows the absorption, dark-field, and transverse shift in both directions on the diffuser plane estimated with cross-correlation from the intensity patterns. For comparison, the result using the speckle-tracking technique on a 1-min-exposure speckle image is

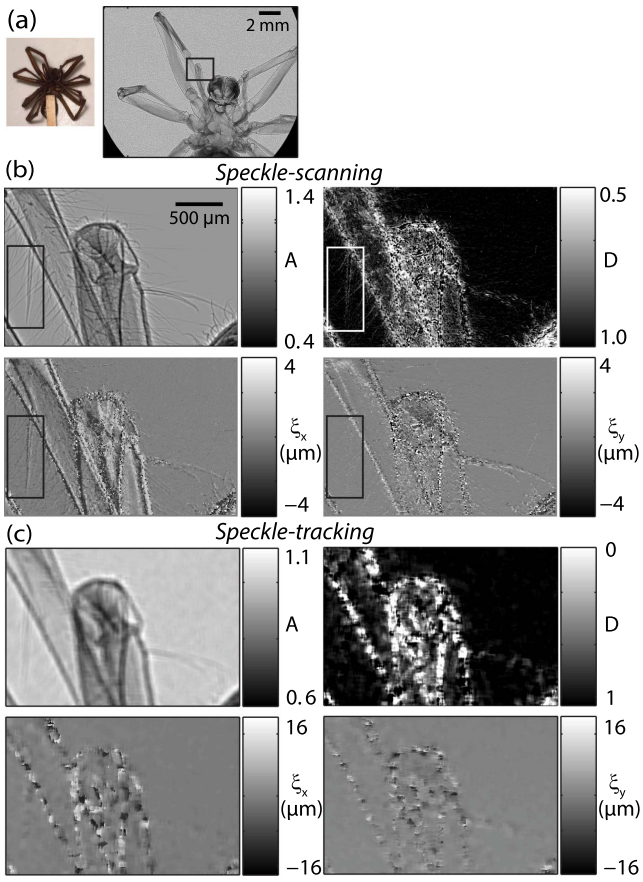

Fig. 4. (a) Photo of the dried spider sample, and one speckle image. Results from the ROI in (a) using the speckle-scanning method are shown in (b), and results from using the speckle-tracking method from one exposure in (c).

presented in Fig. 4(c). The principle for finding the transverse shift is to minimize the difference between the sample image and the reference image within a subset window [9]. The subset window size is chosen empirically as 15 × 15 pixels for a balance of signal-to-noise ratio and resolution. As expected, the speckle-tracking technique gives lower spatial resolution than the speckle-scanning technique since it is restricted by the size of the speckles and of the subset window, which is essentially a low-pass filter. On the other hand, the speckle-tracking technique requires much shorter exposure time, and thus has an advantage in applications that require high-speed phase-contrast imaging but not high spatial resolution. For the speckle-scanning technique, the exposure time can be reduced for instance by reducing the number of scan steps. One approach is to use a 1D scan [16] instead of a 2D raster scan. The marked ROI in Fig. 4(b) is enlarged and shown in Fig. 5 with the same gray scale, where a fine hair of a diameter around 7 μm can be distinguished. The diameter of the hair is estimated by comparing the absorption image and its edge enhancements to simulated objects [17]. Seen from Fig. 5, ξ_y appears to give a lower signal than ξ_x even for fine hair oriented more horizontally. One reason is that the source spot is a bit elongated, so the spatial coherence in the y direction is worse than in the x direction. The thermal drift of the source might also affect the y direction more, and the linear stage used for

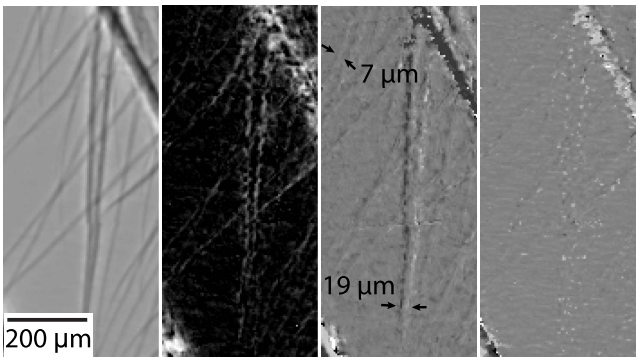

Fig. 5. Enlarged ROIs from Fig. 4(b). From left to right are absorption, dark-field, and transverse shift in x and y directions.

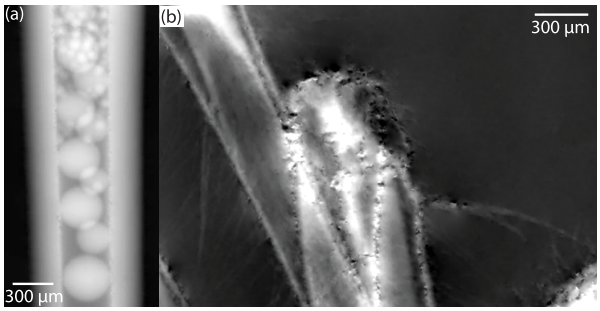

Fig. 6. Phase map of (a) the plastic phantom in Fig. 3 and (b) the spider leg in Fig. 4, calculated by integrating the phase gradients in two directions using a regulated iterative method [9].

scanning vertically has been found to be less stable than the one for scanning horizontally according to the feedback, possibly due to higher load.

The phase maps of the phantom and the spider are shown in Fig. 6. They are integrated from the gradients g_x and g_y by minimizing the weighted sum of squares deviation [9]

$$\chi^2 = \sum_{i,j} \frac{1}{r_{i,j}^2}[(\phi_{i+1,j} - \phi_{i,j} - g_{y,i,j})^2 + (\phi_{i,j+1} - \phi_{i,j} - g_{x,i,j})^2], \quad (3)$$

where ϕ is the phase, and $r_{i,j}$ is the residual of cross-correlation at pixel (i, j). Modified from [9], the residual $r_{i,j}$ is evaluated as

$$r_{i,j}^2 = \sum_{k,l}[A_{i,j} I_{\mathrm{ref},i,j}(k + \delta_{y,i,j}, l + \delta_{x,i,j}) - I_{\mathrm{samp},i,j}(k, l)]^2, \quad (4)$$

where (k, l) are the local coordinates in the scan intensity pattern, and $A_{i,j}$ is the absorption value at pixel (i, j). The reference scan pattern is transversely shifted with the local shift $\delta_{i,j}$ (in pixel) obtained from cross-correlation and then multiplied by $A_{i,j}$ to represent the estimated value under the assumption of only absorption and in-plane local shift. Thus the residual square r^2 is the sum of the square difference between the scan sample image value and the estimated value over all (k, l). Using such a weighting factor $1/r^2$ in the integration can reduce the error from low-quality phase-gradient pixels and hence low-frequency artifacts compared to the commonly used Fourier integration method [18].

In summary, we have applied the speckle-based scanning technique on a laboratory source for the first time, and demonstrated its potential using a plastic phantom and a biological sample. Structures down to around 7 μm can be distinguished, significantly smaller than the speckle-tracking method. This technique can be of interest for multimodal high-resolution laboratory phase-contrast imaging. Similar studies on dark-field imaging [16] and on wavefront reconstruction [19] have the potential to be performed in the laboratory.

Knut och Alice Wallenbergs Stiftelse (Knut and Alice Wallenberg Foundation); Vetenskapsrådet (Swedish Research Council).

We thank Sebastien Berujon for the advice on the implementation of the speckle-scanning technique and Pierre Thibault for the help with the phase-integration codes.

REFERENCES

1. S. W. Wilkins, T. E. Gureyev, D. Gao, A. Pogany, and A. W. Stevenson, Nature **384**, 335 (1996).
2. F. Pfeiffer, T. Weitkamp, O. Bunk, and C. David, Nat. Phys. **2**, 258 (2006).
3. K. S. Morgan, D. M. Paganin, and K. K. W. Siu, Appl. Phys. Lett. **100**, 124102 (2012).
4. S. Berujon, E. Ziegler, R. Cerbino, and L. Peverini, Phys. Rev. Lett. **108**, 158102 (2012).
5. H. C. Wang, S. Berujon, I. Pape, and K. Sawhney, J. Phys. Conf. Ser. **463**, 012042 (2013).
6. S. Berujon, H. C. Wang, and K. Sawhney, Phys. Rev. A **86**, 063813 (2012).
7. M. Stockmar, P. Cloetens, I. Zanette, B. Enders, M. Dierolf, F. Pfeiffer, and P. Thibault, Sci. Rep. **3**, 1927 (2013).
8. M. Stockmar, I. Zanette, M. Dierolf, B. Enders, R. Clare, F. Pfeiffer, P. Cloetens, A. Bonnin, and P. Thibault, Phys. Rev. Appl. **3**, 014005 (2015).
9. I. Zanette, T. Zhou, A. Burvall, U. Lundstrom, D. H. Larsson, M. Zdora, P. Thibault, F. Pfeiffer, and H. M. Hertz, Phys. Rev. Lett. **112**, 253903 (2014).
10. I. Zanette, T. Weitkamp, T. Donath, S. Rutishauser, and C. David, Phys. Rev. Lett. **105**, 248102 (2010).
11. D. H. Larsson, U. Lundström, U. K. Westermark, M. Arsenian Henriksson, A. Burvall, and H. M. Hertz, Med. Phys. **40**, 021909 (2013).
12. R. Cerbino, L. Peverini, M. A. C. Potenza, A. Robert, P. Bosecke, and M. Giglio, Nat. Phys. **4**, 238 (2008).
13. J. Y. Stein, *Digital Signal Processing a Computer Science Perspective* in Wiley Series in Telecommunications and Signal Processing (Wiley, 2000).
14. B. Pan, K. M. Qian, H. M. Xie, and A. Asundi, Meas. Sci. Technol. **20**, 062001 (2009).
15. E. M. C. Jones, M. N. Silberstein, S. R. White, and N. R. Sottos, Exp. Mech. **54**, 971 (2014).
16. H. Wang, Y. Kashyap, and K. Sawhney, Phys. Rev. Lett. **114**, 10391 (2015).
17. U. Lundström, D. H. Larsson, A. Burvall, P. A. Takman, L. Scott, H. Brismar, and H. M. Hertz, Phys. Med. Biol. **57**, 2603 (2012).
18. C. Kottler, C. David, F. Pfeiffer, and O. Bunk, Opt. Express **15**, 1175 (2007).
19. S. Berujon, H. C. Wang, S. Alcock, and K. Sawhney, Opt. Express **22**, 6438 (2014).